Proceedings of ASME Turbo Expo 2011
GT2011
June 6-10, 2011, Vancouver, British Columbia, Canada

GT2011-45169

HEAT TRANSFER IN AN OBLIQUE JET IMPINGEMENT CONFIGURATION WITH VARYING JET GEOMETRIES

Simon Schueren*
Florian Hoefler
Jens von Wolfersdorf
Institute of Aerospace Thermodynamics (ITLR)
Universität Stuttgart
Pfaffenwaldring 31
D-70569 Stuttgart, Germany
eMail: simon.schueren@itlr.uni-stuttgart.de

Shailendra Naik
Alstom Power
Brown Boveri Strasse 7
CH-5401 Baden, Switzerland

ABSTRACT

Experimental and numerical heat transfer results in a trapezoidal duct with two staggered rows of inclined impingement jets are presented. The influence of changes in the jet bore geometry on the wall heat transfer is examined. The goal of this project is to minimize the thermal load in an internal gas turbine blade channel and to provide sufficient cooling for local hot spots.

The dimensionless pitch is varied between $p/d_{jet} = 3$ - 6. *For* $p/d_{jet} = 3$, *cylindrical as well as conically narrowing bores with a cross section reduction of 25% and 50%, respectively, are investigated. The studies are conducted at* $10,000 \leq Re \leq 75,000$. *Experimental results are obtained using a transient thermochromic liquid crystal technique. The numerical simulations are performed solving the RANS equations with FLUENT using the low-Re k-ω-SST turbulence model.*

The results show that for greater pitch, the decreasing interaction between the jets leads to diminished local wall heat transfer. The area averaged Nusselt numbers decrease by up to 15 % for $p/d_{jet} = 4.5$, *and up to 30 % for* $p/d_{jet} = 6$, *respectively, if compared to the baseline pitch of* $p/d_{jet} = 3$. *The conical bore design accelerates the jets, thus increasing the area-averaged heat transfer for identical mass-flow by up to 15% and 30% for the moderately and strongly narrowing jets, respectively. A dependency of the displacement between the Nu maximum and the geometric stagnation point from the jet shear layer is shown.*

*Address all correspondence to this author.

NOMENCLATURE

A	[m^2]	Area
c	[J/kgK]	specific heat capacity
c_D	[-]	discharge coefficient
d	[m]	bore diameter
h	[W/m^{2}K]	heat transfer coefficient
I	[-]	turbulence intensity
k	[W/mK]	thermal conductivity
l	[m]	length
Nu	[-]	Nusselt number
p	[m]	bore pitch
$\dot{Q}$	[W]	heat flow
$\dot{q}$	[W/m^2]	specific heat flux
Re	[-]	Reynolds number
s	[m]	circumferential coordinate
s'	[-]	dimensionless circumferential coordinate
T	[K]	temperature
t	[s]	time
v	[m/s]	velocity
y^+	[-]	dimensionless wall distance
z	[m]	jet-to-plate distance
φ	[-]	angle
Θ	[-]	dimensionless temperature
ρ	[kg/m^3]	density
σ	[-]	standard deviation
ω	[1/s]	vorticity

Subscripts

0	with reference to initial conditions
A	with reference to wall A
A1	with reference to impingement jet row A1
A2	with reference to impingement jet row A2
B	with reference to wall B
C	with reference to wall C
D	with reference to wall D
F	with reference to the fluid
in	with reference to the impinging jet bore entry
jet	with reference to the impinging jets
mean	with reference to area averaged values
out	with reference to the impinging jet bore exit
P	with reference to perspex
t	with reference to total conditions
W	with reference to the wall

INTRODUCTION

The continuous pursuit of increasing gas turbine efficiency, motivated by rising fuel cost, diminishing resources, and economic requirements, leads to higher turbine inlet temperatures. As a result, blades and vanes of modern gas turbines are thermally highly loaded components which need to be intensively cooled in order to extend their lifespan. Thus, profound knowledge of cooling performance is essential for safely improving the overall efficiency of the turbine. Modern design concepts aim to achieve these goals by minimizing cooling air mass flows while dealing with local hot spots. Several authors have given an overview of state of the art technology for internal gas turbine blade cooling, e.g. [1, 2].

Impingement cooling is a viable method for gas turbine components because high heat transfer coefficients can be achieved in order to deal with local hot spots. A comprehensive overview of jets impinging on solid surfaces can be found in [3]. More recent reviews were given by Han and Goldstein [4] and by Zuckerman and Lior [5, 6], where the latter concentrated mainly on numerical analysis. Weigand and Spring [7] summarized the heat transfer characteristics of multiple jet systems.

The present study deals with the impact of two geometric parameters of an oblique impingement configuration on heat transfer. On the one hand, the pitch p between the impingement bores was varied. On the other hand, cylindrical bores were compared with conically narrowing ones. Various authors studied the influence of p on the jet heat transfer. Hollworth and Berry [8] investigated large hole pitch values of $10 \leq p/d_{jet} \leq 25$ for Reynolds numbers between 3,000 and 35,000 and found the local Nusselt numbers to decline with growing pitch. However, if one considers the larger area supplied by each individual jet, higher p results in an increased total heat flow per amount of cooling air. This trend was also confirmed by Huber and Viskanta [9] for

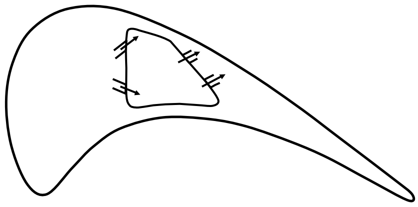

FIGURE 1: SCHEMATIC OF AN IMPINGEMENT COOLED MID-CHORD PASSAGE OF A TURBINE BLADE

$4 \leq p/d_{jet} \leq 8$ and 3,500 $\leq Re \leq$ 20,400 as well as Haiping et al. [10] for $5 \leq p/d_{jet} \leq 15$ and 7,000 $\leq Re \leq$ 20,000. Weigand and Spring [7] listed further studies with similar results.

There are only few publications on conically narrowing impingement bores. Pan et al. [11] compared water jets through a long cylindrical nozzle and a narrowing nozzle with rounded contours. The former yielded slighly higher Nu in the stagnation region. However, both nozzles had the same outlet diameter, which Re referred to. In contrast, the bores in the present investigation have the same inlet diameter. If the Reynolds numbers in [11] were formed with the nozzle inlet diameter, heat transfer for the contoured nozzle would be higher for comparable Re. Brignoni and Garimella [12] conducted experiments comparing a cylindrical nozzle with two different chamfered orifices ending in a cylindric cross-section with the same diameter. They measured slightly increasing heat transfer as well as a significant reduction of pressure loss with the conical nozzles. Royne and Dey [13] investigated water jets with both a cylindrical and a conical bore. The conically narrowed orifice yielded the largest averaged Nu and the highest values for c_D.

The configuration examined in the present paper is related to an advanced mid-chord cooling passage for gas turbine blades. Figure 1 shows an example of such a turbine blade with the impingement cooled passage. It is characterized by a combination of wall-integrated impingement jets with local flow extraction. The jets are directed toward the pressure and suction sides of the blade. The outflow is solely obtained through vent holes in a staggered arrangement to the jets and hence no significant crossflow is generated.

For the experiments incorporated in this study, the impingement jet bore pitch was varied between $3\,d_{jet}$ and $4.5\,d_{jet}$. The CFD simulations additionally included $p = 6\,d_{jet}$. For $p/d_{jet} = 3$, cylindrical bores were compared with conical bores featuring 25% and 50% cross-section reduction, respectively (in the following referred to as conical bores I and II, respectively). For all setups, Reynolds numbers between 10,000 and 75,000 were investigated.

Although the investigated geometry is somewhat specific, it might be representative for future advanced turbine blade cooling passages. The aim of this contribution is to experimentally analyze the complex heat transfer phenomena for varying geo-

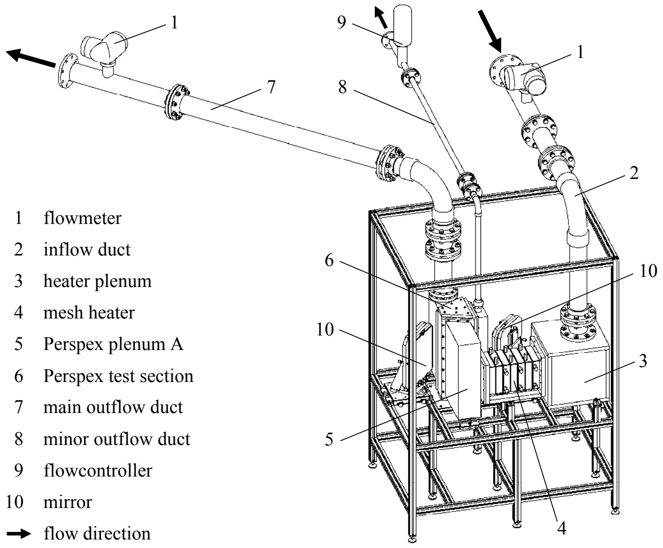

FIGURE 2: SCHEMATIC OF THE EXPERIMENTAL FACILITY

metric parameters and to investigate the numerical predictability of these variations using Reynolds-averaged Navier-Stokes (RANS) simulations. These are frequently applied in the industrial design process because of their comparatively low computational cost and satisfying accuracy.

EXPERIMENTAL SETUP AND PROCEDURES

Test Section and Geometry

The test facility consists of a rotary blower followed by a water radiator which supplies a constant air flow at around 20°C. At a maximum absolute pressure of 1.6 bar a mass flow of 200 g/s can be realized. After passing the heater plenum, the flow is led through a mesh heater. The mesh heater consists of six steel wire cartridges connected in series and charged with a total of 12 kW electrical power. It is designed to obtain air temperature steps of up to 60 K at the highest mass flow rates. The experimental facility is shown in Fig. 2. Details about the instrumentation of the experimental rig can be found in [14] and [15].

Figure 3a shows the baseline configuration test section. After leaving the mesh heater, the air flow enters plenum A, the supply chamber for the impingement jets. Two rows of inclined bores in wall A lead the jets into the passage. The outflow from the test section is realized through two rows of bores towards plenum B and the main outflow duct. Plenums A and B as well as all components of the test section are made of perspex to ensure low thermal conductivity and optical accessibility for the heat transfer measurements. The jet rows A1, A2, B1, and B2 in Fig. 3b are composed of of seven inclined circular bores. Rows A1 and B2 as well as A2 and B1, respectively, are positioned

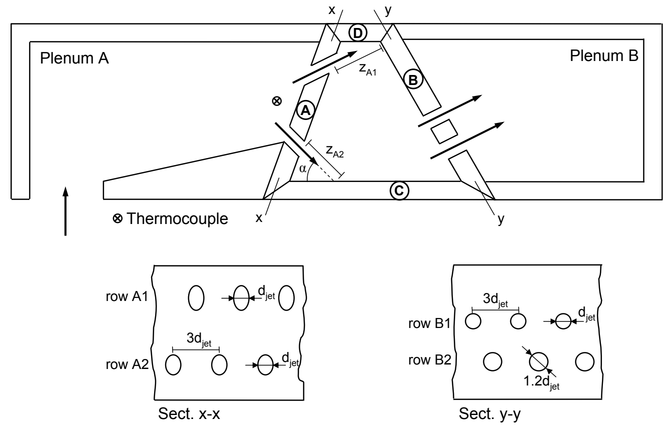

(a) SCHEMATIC OF THE TEST SECTION GEOMETRY IN ITS BASELINE CONFIGURATION

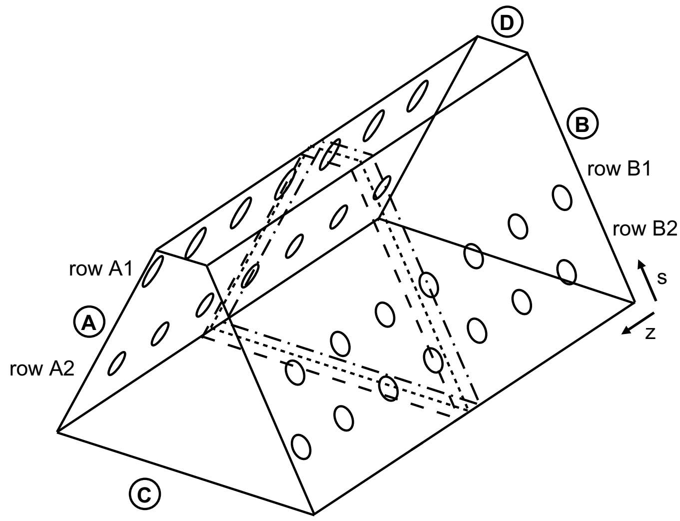

(b) SCHEMATIC OF THE TEST CHANNEL

FIGURE 3: EXPERIMENTAL SETUP

in-line. The rows A1, A2, and B1 have the same diameter d_{jet} whereas the diameter of row B2 is $1.2\,d_{jet}$. The presented results are related to the jet Reynolds number *Re*, which is based on the jet diameter d_{jet} and assumes an equally distributed mass flow through all jets. The jets of row A1 impinge with an incident angle of 30° on wall D. Likewise, the incident angle of the jets of row A2 is 30° relative to wall C. The dimensionless jet-to-plate distance z/d_{jet} for row A1 is 2.56 and for row A2 3.95. Figure 3b introduces a circumferential coordinate s moving counter-clockwise around all channel walls.

The different bore geometries with their respective dimensionless legth and diameter ratios as well as the impingement angles are shown in Fig. 4.

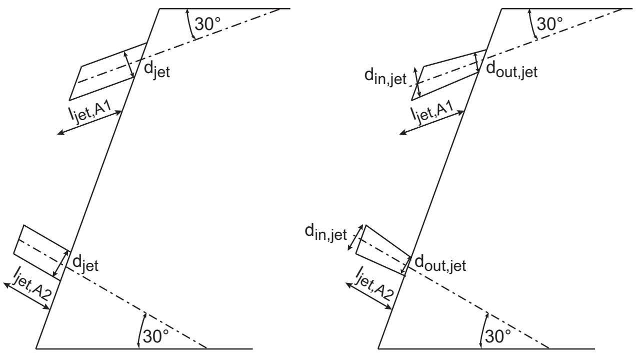

(a) CYLINDRICAL BORES (b) CONICAL BORES

	$l_{jet,A1}/d_{(in)\,jet}$	$l_{jet,A2}/d_{(in)\,jet}$	$d_{out,jet}/d_{in,jet}$
Cyl. Bores	3.89	2.60	1
Con. Bores I	3.89	2.60	0.87
Con. Bores II	3.89	2.60	0.71

FIGURE 4: SKETCH OF DIFFERENT BORE CONFIGURATIONS WITH GEOMETRIC DATA

Measurement Techniques and Data Reduction

To measure heat transfer, a transient thermochromic liquid crystal (TLC) method [16] was used. This technique is based on the temperature dependent color change of a layer of liquid crystals applied on every investigated surface. Since all walls were observed from the outside, the TLCs were sprayed directly onto each plate and covered with a layer of black coating to enhance contrast. A narrow bandwidth type ($38°C - 39°C$) of TLCs was used for all experiments.

Based on the assumption of one-dimensional heat conduction with a convective boundary condition, a step-change in the fluid temperature leads to a time dependent wall temperature distribution. Starting from a well-known initial model temperature T_0, the wall temperature T_W responds to the sudden rise of the fluid temperature T_F. Once the wall temperature reaches the indication temperature the TLCs begin to reflect incident light within the color spectrum. A separate calibration of the liquid crystals provides a relationship between the maximum green intensity and the TLC temperature.

For an ideal temperature step change the time-dependent wall temperature distribution can be described by the semi-infinite wall solution [17]:

$$\Theta = \frac{T_W - T_0}{T_F - T_0} = 1 - exp\left(\frac{h^2\, t}{k_P\, \rho_P\, c_P}\right) erfc\left(\sqrt{\frac{h^2\, t}{k_P\, \rho_P\, c_P}}\right) \quad (1)$$

To account for the non-ideal temperature rise, the Duhamel's principle is applied to Eqn. (1) as described in [18]. For impingement heat transfer problems it is common to define the heat transfer coefficient relative to the jet total temperature [3]. In the present investigation, the total temperature was measured in plenum A with a thermocouple close to the jets and applied for the evaluation of all test section walls. The position of the thermocouple is indicated in Fig. 3a. To avoid additional optical blockage on plate A, we used no more than one thermocouple to capture the fluid temperature. The experimental data has been evaluated using an ITLR in-house program. Poser et al. [19] described details about the applied data analysis.

The experiments have been performed with various temperature steps (see Hoefler et al. [20]). The results have proven to be independent of the chosen temperature level within experimental uncertainties.

Uncertainty Analysis

A measurement uncertainty analysis for the heat transfer measurements was carried out following the method outlined by Moffat [21]. The uncertainties of the measured input parameters are listed in Tab. 1 with a confidence interval of 95%. The given uncertainty for the fluid temperature measurements covers an increased uncertainty level of thermocouples for heated flow. The uncertainty for T_W arises from the TLC calibration procedure. For the overall uncertainty calculation of the heat transfer coefficient *h*, the resulting equation with Duhamel's principle was taken into account. Furthermore, the overall uncertainties are dependent on the value of *h*, with increasing values resulting in higher uncertainties. Hence, the root sum square uncertainty in the presented work for the highest heat transfer rates was calculated to $\pm 13\%$. The mass flow measurements determining *Re* have an uncertainty of $\pm 2.5\%$, according to the manufacturer.

A transient CFD investigation showed that in an area of up to 1.5 bore diameters around the impingement and extraction holes, sharp edges and strong temperature gradients cause lateral heat conduction. In these regions, the assumption of one-dimensional heat conduction can not be upheld. Hence, the uncertainty of the results obtained with the TLC method will be higher in these areas, which, however, are not the main focus of the heat transfer analysis in our case. A closer investigation of the effects of lateral heat conduction on wall C following the method of Kingsley-Rowe et al. [22] yielded a maximum local difference of 4% between the one-dimensional Biot number and a corrected Biot number which includes lateral heat conduction effects. The average discrepancy lies well below 1%.

NUMERICAL SETUP AND PROCEDURES

The numerical calculations were conducted with the commercial finite-volume-solver FLUENT (version 12.1) using the low-*Re* k-ω-SST turbulence model. This model has proven appropriate for RANS simulations of jet impingement heat transfer, see Zuckerman and Lior [5], Hofmann et al. [23], Rao et al. [24] and Zu et al. [25]. In order to minimize the computa-

TABLE 1: UNCERTAINTIES FOR HEAT TRANSFER MEASUREMENTS

Quantity	k [W/mK]	ρ [kg/m³]	c [J/kgK]
Uncertainty	$\pm 5\%$	$\pm 1\%$	$\pm 1\%$
Quantity	T_W, T_0 [K]	T_F [K]	t [s]
Uncertainty	± 0.2	± 0.4	± 0.1

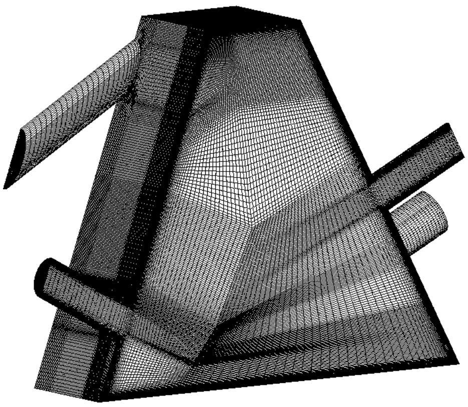

FIGURE 5: NUMERICAL GRID

tional effort, a symmetrical channel segment comprising half a bore of each row was discretized, as shown in Fig. 5

The structured hexahedral meshes were generated with the commercial software ANSYS ICEMCFD (version 12.1). The boundary layer was resolved with $y^+ \leq 2$, as required by the turbulence model. The Grid Convergence Index (GCI) according to Roache [26] was determined in order to quantify the discretization error and study the influence of grid resolution. For the case of $p/d_{jet} = 6$ and $Re = 45,000$, the GCI for Nu averaged over all channel walls is 3.46%. Table 2 lists relevant data for the grids used for this study.

TABLE 2: GRID DATA FOR GCI-CALCULATION

	Grid 1	Grid 2	Grid 3
number of cells	5,313,570	2,450,253	1,113,041
target wall max. y^+	0.826	1.057	1.356
max. aspect ratio	608	444	547
min. cell angle	15.0°	15.0°	15.0°

The fluid density is modeled according to the ideal gas law, thus depending on local values of pressure and temperature. All transport equations were solved with second order accuracy schemes and the SIMPLE-algorithm was used for the pressure-velocity coupling. The calculations were parallelized fourfold and required 5.5 GB RAM and approx. 100 h computing time on an Intel Xeon quad core 3.2 GHz processor. In order to achieve the desired convergence criteria, such as sufficiently constant monitor values for relevant hydrodynamic and thermal quantities as well as residuals below 10^{-5}, about 20,000 iterations were necessary.

At the inlet, mass flow rates for each row are defined, resulting in block-shaped velocity profiles. The total mass flow is not distributed equally between rows A1 and A2, but divided according to the experimentally measured discharge coefficients c_D through the orifices, see Tab. 3 (details about the c_D-measurements can be found in [14]). The mass flow distributions are listed only for the representative Reynolds number of 45,000, because the values for other Re are very similar. Since no experiments could be conducted for $p/d_{jet} = 6$, the mass flow distributions from $p/d_{jet} = 4.5$ were assumed for these cases.

TABLE 3: MASS FLOW DISTRIBUTION FOR $Re = 45,000$

		jet row	
Geometry		A_1	A_2
$p/d_{jet} = 3$	cyl. bores	46.2%	53.8%
	con. bores I	48.4%	51.6%
	con. bores II	49.1%	50.9%
$p/d_{jet} = 4.5$		46.2%	53.8%
$p/d_{jet} = 6$		46.2%	53.8%

The flow enters the domain with a static temperature of 55°C and a turbulence intensity according to $I = 0.16 Re^{1/8}$. All channel walls are modeled isothermal with no-slip conditions and a constant temperature of 38°C, which corresponds to the indication temperature of the thermochromic liquid crystals. The outlet bores of rows B1 and B2 are openings against ambient pressure, thus allowing outflow and backflow into the cavity. The jet total temperature at the inlet serves as reference temperature for determining the heat transfer coefficient h, see Eqn. (2).

$$h = \frac{\dot{q}}{(T_{t,jet} - T_W)} \quad (2)$$

Heat transfer results are given in dimensionless form, using the Nusselt number according to Eqn. (3).

$$Nu = \frac{h\, d_{jet}}{k_F} \quad (3)$$

RESULTS

The present paper comprises experimental and numerical analyses of the wall heat transfer in the duct described above.

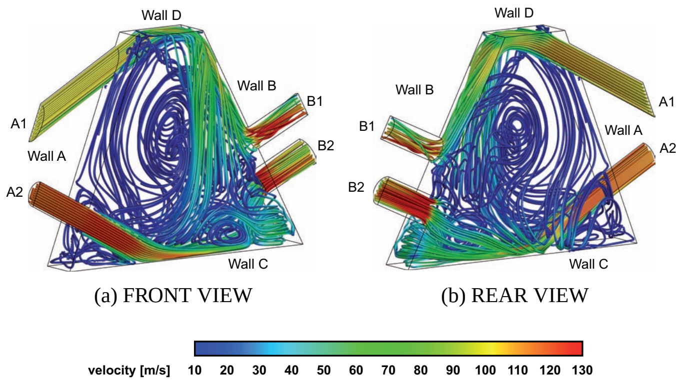

(a) FRONT VIEW (b) REAR VIEW

FIGURE 6: STREAMLINES FOR $p/d_{jet} = 3,\ Re = 75,000$

The TLC method yields locally resolved results for all channel walls. These are compared with numerically gained data. In addition, laterally averaged Nusselt numbers are presented. The simulations provide information about the flow field which strongly influences the heat transfer, but is not determined experimentally.

Flow Field

Figure 6 shows streamlines for $p/d_{jet} = 3$ and $Re = 75,000$. The jets impinge on their respective target walls and run along them. The jet originating from row A1 is deflected subsequently and impinges again on Wall B. A large center vortex as well as a smaller corner vortex between walls B and C are clearly detectable. Within these vortices, flow velocities are relatively low, whereas velocity maxima occur in the regions close to the outlet openings due to the strong streamline deflection. This goes along with significant flow contraction and streamline separation, see Fig. 6b. These features are stronger in row B1 because the flow experiences a deflection of nearly 90° after following wall B. The zone between walls A and C is dominated by scarce fluid exchange with the rest of the cavity and low flow velocities.

Figure 7 shows contours of the vorticity magnitude $|\vec{\omega}| = |\nabla \times \vec{v}|$. Three planes for each bore pitch, 3, 4.5, and 6 jet diameters, respectively, are displayed. These correspond to the three cutting planes in Fig. 3 (dashdotted line for Figs. 7a, 7d, and 7g, dotted line for Figs. 7b, 7e, and 7h, and dashed line for Figs. 7c, 7f, and 7i). The rotation afflicted boundary layers in the inlet bores can be seen. Upon entering the cavity, friction with the ambient fluid causes shear layers of high vorticity. The jets widen whereas the potential core, characterized by low vorticity magnitude, narrows.

In Figs. 7b, 7e, and 7h, one sees raised levels of $|\vec{\omega}|$ in the stagnation region between the jets. The secondary impingement of the jets from row A1 on wall B already observed in Fig. 6 shows again in Figs. 7c, 7f, and 7i. When the jet impinges on wall B, its potential core is still intact. The high levels of $|\vec{\omega}|$ in the outlet bores indicate flow separation. The reduction of $|\vec{\omega}|$ with growing p/d_{jet}, which can be observed in Figs. 7b, 7e, and 7h gives proof to diminished interaction between individual jets. The flow phenomena for $Re = 75,000$ occur similarly for other Reynolds numbers and geometry configurations. Thus they serve to explain the heat transfer results in the following sections.

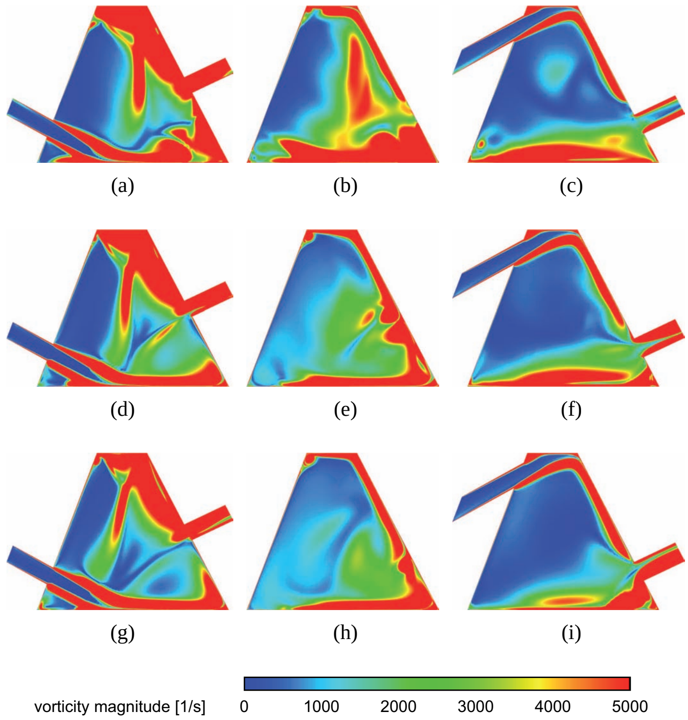

(a) (b) (c) (d) (e) (f) (g) (h) (i)

FIGURE 7: VORTICITY MAGNITUDE AT $Re = 75,000$ IN SLIDES THROUGH JET AXES AND BETWEEN JETS: (a)-(c) $p/d_{jet} = 3$, (d)-(f) $p/d_{jet} = 4.5$, (g)-(i) $p/d_{jet} = 6$

Heat Transfer

Pitch Variation Figure 8 exhibits contours of experimentally determined Nu. The evaluation focuses on the center segment of the channel with a width of $2.5\,p$ in order to reduce the impact of the side walls. The local Nu-distributions are normalized with the respective area-averaged values for each wall, which are listed in the table. These plots show no significant qualitative differences in heat transfer characteristics for the different pitches. Especially the egg-shaped maxima on wall C and the horseshoe-shaped contours on target wall D remain qualitatively unchanged. The blanked regions on walls A and B are caused by the inlet and outlet bores (which appear distorted due to the non-perpendicular camera perspective), respectively, and a

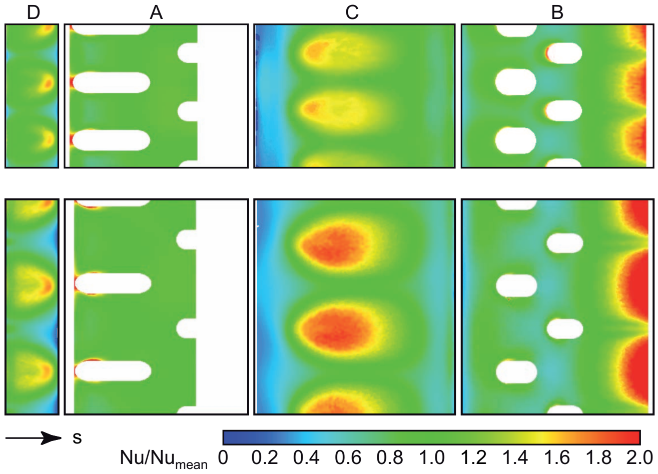

Nu_{mean}	Wall A	Wall B	Wall C	Wall D
$p/d_{jet} = 3$	44.1	94.3	82.2	124.3
$p/d_{jet} = 4.5$	34.6	86.2	81.1	112.1

FIGURE 8: EXPERIMENT: LOCAL NUSSELT NUMBER RATIOS AT $Re = 45,000$, FROM TOP TO BOTTOM: $p/d_{jet} = 3$, $p/d_{jet} = 4.5$, AREA AVERAGED NUSSELT NUMBERS Nu_{mean}

wedge in plenum A (see Fig. 3a), which prevent optical access.

Nusselt number maxima occur in the stagnation regions on walls C and D as well as on wall B, where the jets from row A1 impinge again after being deflected. For $p/d_{jet} = 4.5$, the areas of high Nusselt number extend further downstream while zones of low heat transfer arise between the jets. The latter, which is caused by the diminishing jet interaction, is also visible on wall C, where the Nu maximum increases for larger bore pitch, while the area-averaged heat transfer remains almost unaltered.

The numerical results for different p are shown in Fig. 9. In addition to the experimentally investigated configurations of $p/d_{jet} = 3$ and $p/d_{jet} = 4.5$, CFD simulations were also performed for $p/d_{jet} = 6$. Due to size constraints of the test rig, this pitch could not be investigated experimentally without breaching periodic conditions. As for the experimental results, local Nusselt numbers are normalized with area-averaged values. Qualitatively, the results are in good congruence with the experiments. Again, the contours show no significant changes over p/d_{jet} with their maxima in the stagnation zones, near the edge of walls B and D, and close to the outlet bores. For $p/d_{jet} \geq 4.5$, the zone of high heat transfer widens downstream. In the baseline geometry ($p/d_{jet} = 3$), this is prevented by the increased jet interaction. Like in the experiment, the regions of high Nu show only moderate lateral growth with rising p/d_{jet}, whereas the areas of low Nu expand disproportionately. The increasing distance between the individual jets considerably weakens the corner vortex between

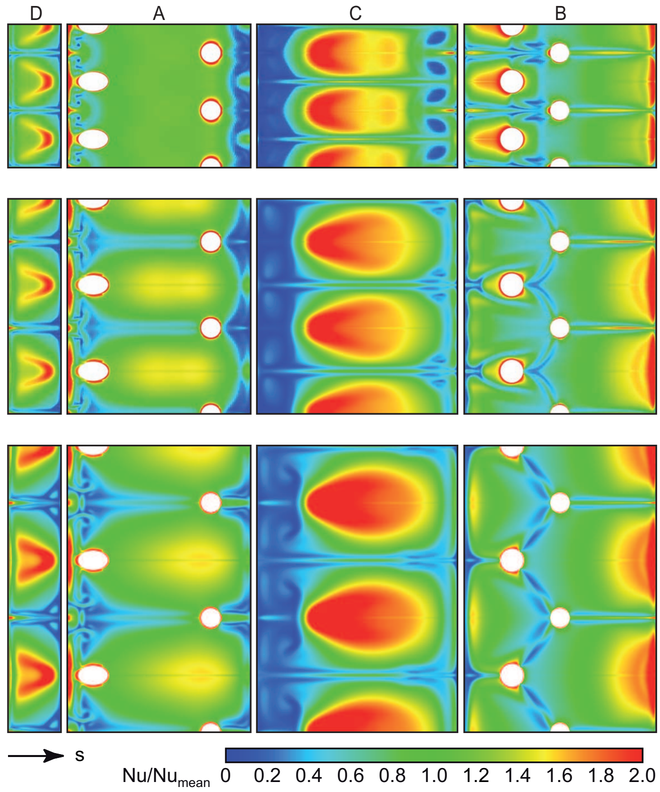

Nu_{mean}	Wall A	Wall B	Wall C	Wall D
$p/d_{jet} = 3$	37.6	114.8	100.5	116.7
$p/d_{jet} = 4.5$	35.2	98.9	90.6	100.3
$p/d_{jet} = 6$	32.4	91.0	81.8	85.1

FIGURE 9: CFD: LOCAL NUSSELT NUMBER RATIOS AT $Re = 45,000$, FROM TOP TO BOTTOM: $p/d_{jet} = 3$, $p/d_{jet} = 4.5$, $p/d_{jet} = 6$, AREA AVERAGED NUSSELT NUMBERS Nu_{mean}

walls B and C which causes a local Nu minimum for $p/d_{jet} = 3$, but hardly affects heat transfer for $p/d_{jet} \geq 4.5$.

Figure 10 displays laterally averaged distributions of Nu. The circumferential coordinate s is made dimensionless with the respective wall length: $s' = s/l_W$. The curves in Figs. 10c and 10d correspond to the contours in Figs. 8 and 9, respectively. The line-averaged experimental Nu-values on wall C nearly collapse for $Re \geq 45,000$. The slightly higher Nu maxima for $p/d_{jet} = 4.5$ are compensated by the larger areas of low Nu. For $Re = 10,000$, heat transfer for $p/d_{jet} = 3$ is about 25% higher than for $p/d_{jet} = 4.5$. On wall D, Nu is nearly independent of p/d_{jet} for $s_D' \leq 0.4$. For $s_D' \geq 0.4$, the zones of low Nu between the jets cause lower averaged Nusselt numbers for larger bore pitch. As on wall C, this effect is more pronounced for the lower Reynolds numbers.

TABLE 4: AREA-AVERAGED NUSSELT NUMBERS AND ABSOLUTE HEAT FLOW AT $Re = 45,000$, NORMALIZED WITH RESULTS FOR $p/d_{jet} = 3$

(a) EXPERIMENTAL RESULTS

	A	$\overline{Nu_C}$	$\overline{Nu_D}$	$\dot{Q}_C$	$\dot{Q}_D$
$p/d_{jet} = 3$	1	1	1	1	1
$p/d_{jet} = 4.5$	1.5	0.986	0.902	1.480	1.353

(b) NUMERICAL RESULTS

	A	$\overline{Nu_C}$	$\overline{Nu_D}$	$\dot{Q}_C$	$\dot{Q}_D$
$p/d_{jet} = 3$	1	1	1	1	1
$p/d_{jet} = 4.5$	1.5	0.902	0.859	1.353	1.289
$p/d_{jet} = 6$	2	0.814	0.729	1.629	1.457

The CFD results show a clear trend of declining averaged Nusselt number for increasing p. Lower Nu maxima and growing areas of low Nu add up to this effect. The large fluctuations for $p/d_{jet} = 3$ in the region $0.8 \leq s_C{}' \leq 1$ are attributed to the corner vortex whose intensity declines significantly for larger p. Both the experiments and the simulations show the location of the Nu maximum to shift downstream with rising p/d_{jet}.

While the agreement between experimental and numerical results on wall D is satisfying within the scope of this study, the deviations on wall C are larger. It should be noted that the experimental uncertainty as well as the deviations caused by the different methods (transient experiment vs. steady-state CFD) reach their maxima on wall C. This is why special attention was paid to the measurements on wall C (see Hoefler et al. [20]). The disagreement must to a significant part be ascribed to the experimental results. The overestimation of the Nusselt number by the CFD simulations, especially in the stagnation region, has been reported before, e.g. by Hofmann et al. [23]. Weigand and Spring [7] list further investigations observing the same trend. Two-equation turbulence models tend to overpredict the production of turbulent kinetic energy near the stagnation point, which leads to increased levels of heat transfer.

In addition to locally resolved and line-averaged Nu data, also area-averaged heat transfer results are relevant for the assessment of different bore pitches. Table 4 summarizes these values. Although area-averaged Nusselt numbers decline for larger p, the increased area supplied by each jet gives rise to higher total heat flow, thus using the available cooling air more efficiently. This is consistent with studies conducted by Huber and Viskanta [9] as well as Haiping et al. [10]. However, it is important to keep in mind that the zones of low heat transfer may suffer from high local component temperatures.

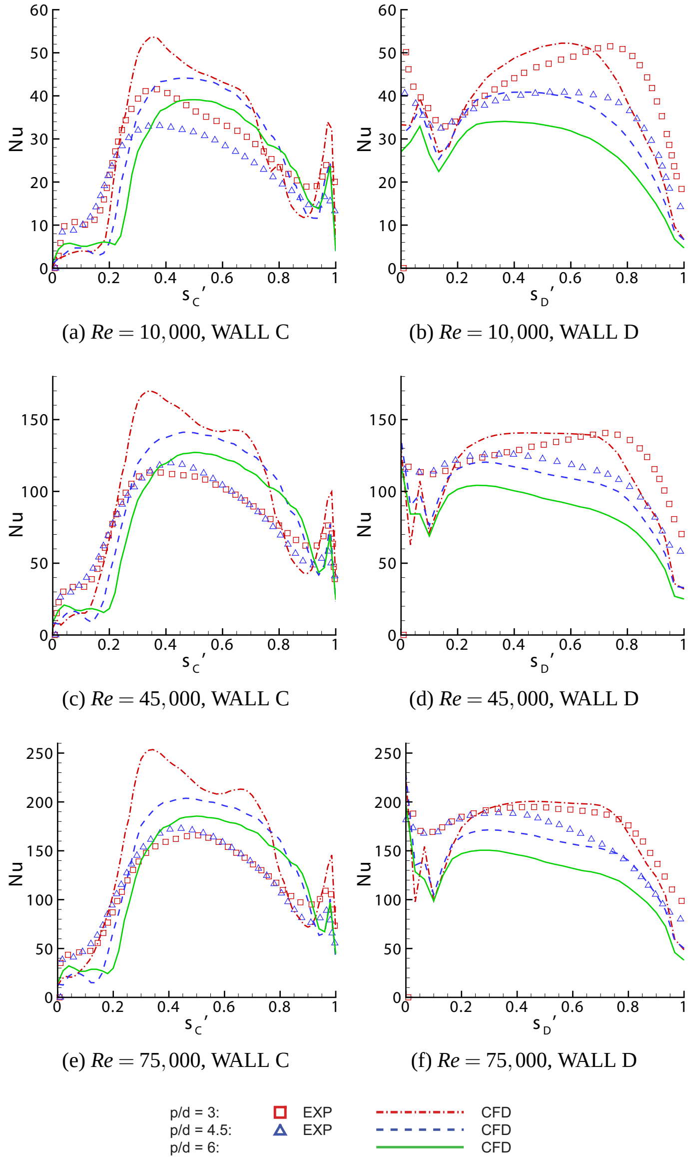

FIGURE 10: LINE-AVERAGED NUSSELT NUMBERS FOR DIFFERENT p/d_{jet} AT VARIOUS REYNOLDS NUMBERS

Bore Shape Variation For the comparison of cylindrical and conical bores, the mass flow through the orifices was kept constant. This leads to increased jet velocities at the bore exit for the conical bores. The nominal Reynolds number is valid for the bore inlet, whereas at the bore exit, Re is elevated by 15.5% (conical bores I) and 41.4% (conical bores II), respectively.

Experimentally obtained Nu contours for the different configurations are displayed in Fig. 11. The intensified heat transfer for the conical bores, caused by the higher jet velocities, is re-

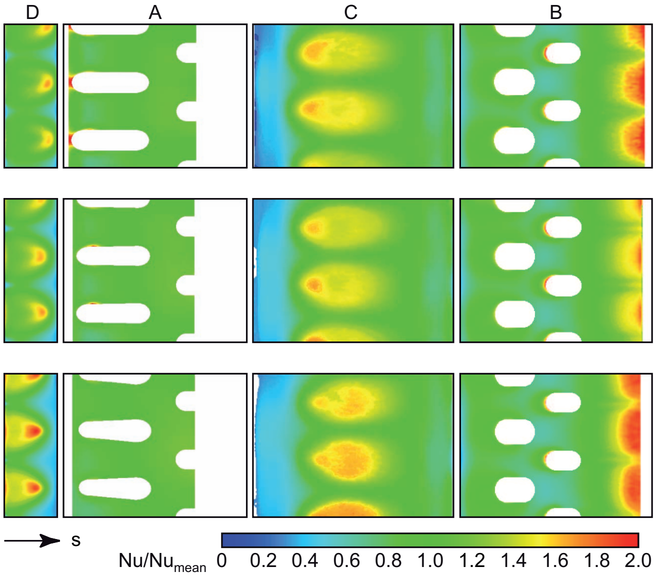

Nu_{mean}	Wall A	Wall B	Wall C	Wall D
cylindrical bores	44.1	94.3	82.2	124.3
conical bores I	47.1	99.4	87.8	126.2
conical bores II	49.5	115.2	99.3	128.3

FIGURE 11: EXPERIMENT: LOCAL NUSSELT NUMBER RATIOS AT $Re = 45,000$, FROM TOP TO BOTTOM: CYLINDRICAL BORES, CONICAL BORES I, CONICAL BORES II, AREA AVERAGED NUSSELT NUMBERS Nu_{mean}

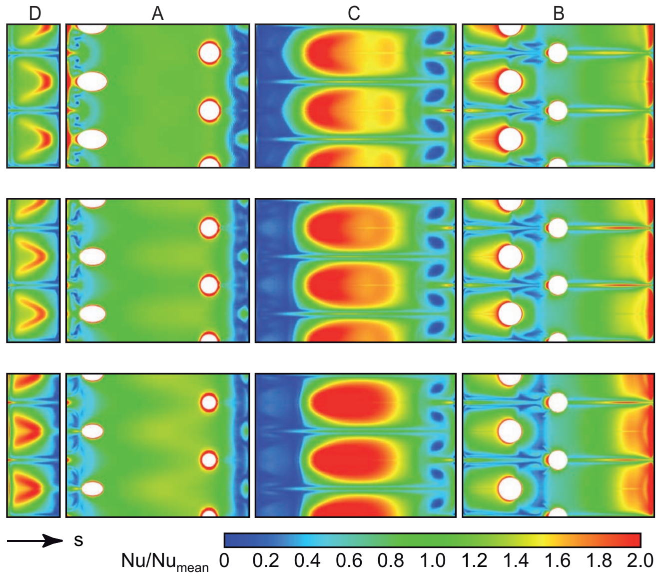

Nu_{mean}	Wall A	Wall B	Wall C	Wall D
cylindrical bores	37.6	114.8	100.5	116.7
conical bores I	47.4	131.4	115.0	130.4
conical bores II	51.1	151.4	129.6	147.9

FIGURE 12: CFD: LOCAL NUSSELT NUMBER RATIOS AT $Re = 45,000$, FROM TOP TO BOTTOM: CYLINDRICAL BORES, CONICAL BORES I, CONICAL BORES II, AREA AVERAGED NUSSELT NUMBERS Nu_{mean}

flected in increased area-averaged heat transfer. However, the contours of Nu/Nu_{mean} for the three bore shapes are similar. Since there are no qualitative changes in the flow field, heat transfer in the regions not directly subjected to the impinging jets remains nearly unchanged. Hence, due to the increased overall heat transfer, Nu/Nu_{mean} decreases slightly in these areas whereas the normalized Nusselt numbers in the stagnation zone rise. In addition to increasing, the Nu maximum is also displaced such that with stronger flow contraction it is located further downstream.

This can also be observed in the CFD results, see Fig. 12. As in the experimental data, the normalized heat transfer contours do not differ significantly in shape. The jet contraction and acceleration cause higher heat transfer downstream of the stagnation region, whereas Nu/Nu_{mean} on the target walls B and C decreases near the edges with wall A.

The line-averaged Nu-plots in Fig. 13 also show smaller differences in the experimentally obtained heat transfer data between the cylindrical bores and those with 25% cross-section reduction, while the strongly narrowed orifices yield clearly higher Nusselt numbers. In the CFD simulations, however, there is a clear trend: the stronger the bore contraction, the higher the Nusselt number level. Both on wall C and on wall D, the downstream displacement of the Nu maximum also shows in the laterally averaged results[1].

Figure 14 serves to understand the displacement of the Nu maximum. Various flow features, such as shear layer onset, jet widening, and contraction of the potential core, have already been mentioned above (see Fig. 7). In addition to the contours of vorticity magnitude, the locations of Nu maximum the and the geometric stagnation point (where the jet axis meets the target wall) are visible. These plots indicate a connection between vorticity and heat transfer. The point of maximum heat transfer coincides with the first impact of the potential core layer on the wall. For the constricted jets this position is located further downstream due to the narrowing of the jet. Thus, the point of maximum Nu lies further downstream and closer to the geometric stagnation point. It also becomes clear that the acceleration of the jet leads to increased levels of vorticity magnitude.

[1] on wall D, 'downstream' corresponds to falling $s_D{}'$ according to the definition of s (see Fig. 3b)

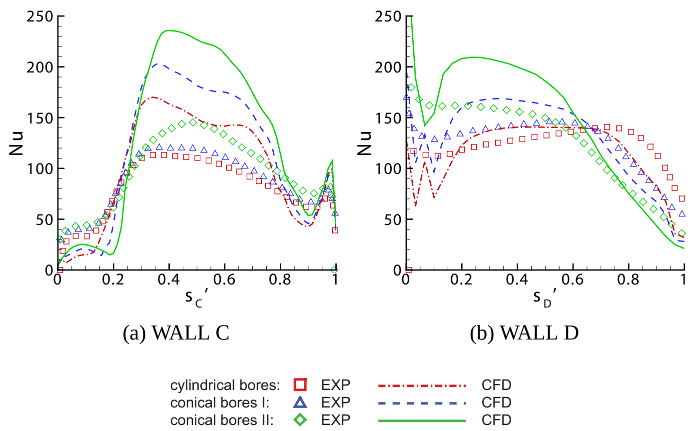

(a) WALL C (b) WALL D

FIGURE 13: LINE-AVERAGED NUSSELT NUMBERS FOR DIFFERENT BORE SHAPES AT $Re = 45,000$

SUMMARY AND CONCLUSIONS

Experimental and numerical heat transfer measurements in a confined impingement cooling configuration with oblique jets are presented. The assembly consists of four trapezoidally arranged walls, one of which holds two staggered rows of inclined jets, each impinging on a different target wall. On the opposing wall, the flow exits the cavity through two mutually staggered rows of outlet openings. The investigated duct is typical for a modern turbine blade midchord cooling channel.

The experimental results were obtained using a transient liquid crystal technique. Steady-state CFD simulations were performed with a low-*Re*-k-ω-SST turbulence model. Spatially resolved Nusselt numbers as well as line-averaged and area-averaged Nusselt numbers are determined. The simulations also help understand the complex flow field in the cavity which drives the heat transfer.

The jets from row A1 are deflected after impinging on wall D and, due to the short length of wall D, impact on wall B. Since the jet potential core is still intact at this secondary impingement, the Nusselt numbers in this region are as high as those in the stagnation regions of the jets.

Two geometric modifications of the baseline configuration are investigated: increased impingement jet pitch and conically narrowing inlet bores. With growing pitch, jet interactions diminish which becomes manifest in decreasing vorticity magnitude. However, the overall flow field remains unaltered, hence no grave qualitative changes in heat transfer are observed. There is a tendency of declining Nusselt number for larger p, which is more pronounced in the CFD results. Between the jets, zones of low Nu arise if the jets are further apart. This leads to lower area-averaged Nusselt numbers, which, however, are outweighed by the increased area supplied by each jet. Thus, for higher p, the cooling air can be used more efficiently.

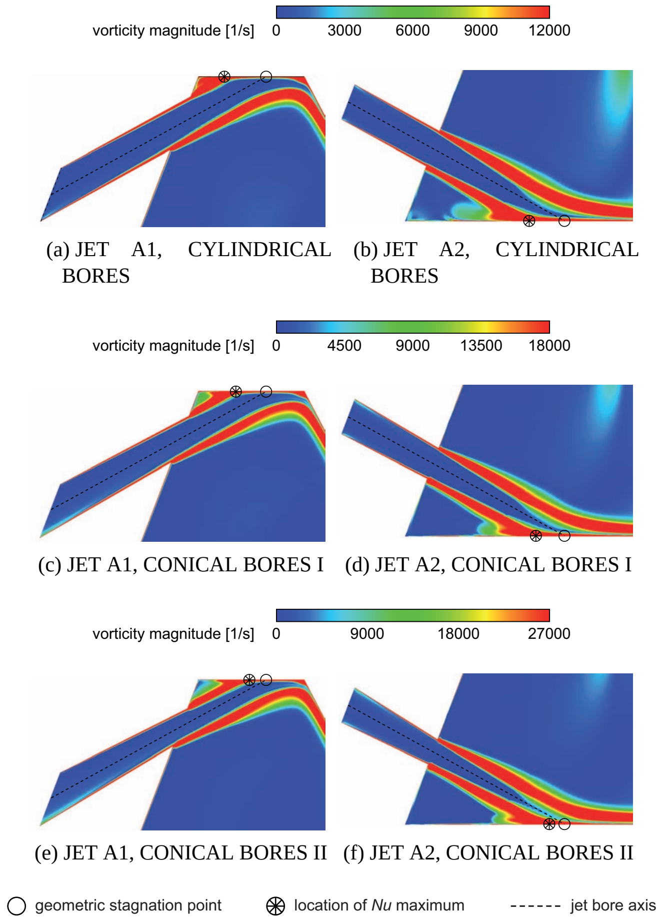

(a) JET A1, CYLINDRICAL BORES (b) JET A2, CYLINDRICAL BORES

(c) JET A1, CONICAL BORES I (d) JET A2, CONICAL BORES I

(e) JET A1, CONICAL BORES II (f) JET A2, CONICAL BORES II

FIGURE 14: CORRELATION BETWEEN JET SHEAR LAYER AND LOCATION OF MAXIMUM NUSSELT NUMBER

The narrowing bore shape accelerates the jets, which increases the stagnation region Nusselt number significantly without strongly affecting the heat transfer in areas not dominated by impingement. The nominal Reynolds number, referring to the bore inlet, is constant, but the effective Reynolds number in the orifice outlet rises. Both higher jet pitch and bore contraction cause a downstream displacement of the Nu maximum.

ACKNOWLEDGMENT

The investigations were conducted as part of the joint research programme COORETEC-turbo in the frame of AG Turbo. The work was supported by the Bundesministerium für Wirtschaft und Technologie (BMWi) as per resolution of the German Federal Parliament under grant number 0327725F. The authors gratefully acknowledge AG Turbo and ALSTOM for their support and permission to publish this paper. The responsibility for the content lies solely with its authors.

REFERENCES

[1] Weigand, B., Semmler, K., and von Wolfersdorf, J., 2001. "Heat Transfer Technology for Internal Passages of Air-Cooled Blades for Heavy-Duty Gas Turbines". *Heat Transfer in Gas Turbine Systems*, ***934***, pp. 179–193.

[2] Han, J. C., and Dutta, S., 2001. "Recent Developments in Turbine Blade Internal Cooling". *Heat Transfer in Gas Turbine Systems*, ***934***, pp. 162–178.

[3] Martin, H., 1977. "Heat and Mass Transfer between Impinging Gas Jets and Solid Surfaces". *Advances in Heat Transfer*, ***13***, pp. 1–60.

[4] Han, B., and Goldstein, R. J., 2001. "Jet-Impingement Heat Transfer in Gas Turbine Systems". *Heat Transfer in Gas Turbine Systems*, ***934***, pp. 147–161.

[5] Zuckerman, N., and Lior, N., 2005. "Impingement Heat Transfer: Correlations and Numerical Modeling". *Journal of Heat Transfer*, ***127***, pp. 544–552.

[6] Zuckerman, N., and Lior, N., 2006. "Jet Impingement Heat Transfer: Physics, Correlations, and Numerical Modeling". *Advances in Heat Transfer*, ***39***, pp. 565–631.

[7] Weigand, B., and Spring, S. Multiple Jet Impingement - A Review. International Symposium on Heat Transfer in Gas Turbine Systems, 9-14 August 2009, Antalya, Turkey.

[8] Hollworth, B. R., and Berry, R. D., 1978. "Heat Transfer from Arrays of Impinging Jets with Large Jet-to-Jet Spacing". *Journal of Heat Transfer*, ***100***(2), pp. 352–357.

[9] Huber, A. M., and Viskanta, R., 1994. "Effect of Jet-Jet Spacing on Convective Heat-Transfer to Confined, Impinging Arrays of Axisymmetrical Air-Jets". *International Journal of Heat and Mass Transfer*, ***37***(18), pp. 2859–2869.

[10] Haiping, C., Jingyu, Z., and Taiping, H., 2000. "Experimental Investigation on Impingement Heat Transfer from Rib Roughened Surface within Arrays of Circular Jets". In Proceedings of ASME Turbo Expo 2000, May 8-11, 2000, Munich, Germany, no. 2000-GT-220.

[11] Pan, Y., Stevens, J., and Webb, B. W., 1992. "Effect of Nozzle Configuration on Transport in The Stagnation Zone of Axisymmetrical, Impinging Free-Surface Liquid Jets .2. Local Heat-Transfer". *Journal of Heat Transfer*, ***114***(4), Nov., pp. 880–886.

[12] Brignoni, L. A., and Garimella, S. V., 2000. "Effects of Nozzle-Inlet Chamfering on Pressure Drop and Heat Transfer in Confined Air Jet Impingement". *International Journal of Heat and Mass Transfer*, ***43***(7), pp. 1133–1139.

[13] Royne, A., and Dey, C. J., 2006. "Effect of Nozzle Geometry on Pressure Drop and Heat Transfer in Submerged Jet Arrays". *International Journal of Heat and Mass Transfer*, ***49***(3-4), pp. 800–804.

[14] Hoefler, F., Schueren, S., von Wolfersdorf, J., and Naik, S., 2009. "Heat Transfer in a Confined Oblique Jet Impingement Configuration". In Proceedings of ASME Turbo Expo 2009, June 8-12, 2009, Orlando, Florida, USA, no. GT2009-59354.

[15] Hoefler, F., Schueren, S., von Wolfersdorf, J., and Naik, S., 2010. "Heat Transfer Characteristics of an Oblique Jet Impingement Configuration in a Passage with Ribbed Surfaces". In Proceedings of ASME Turbo Expo 2010, June 14-18, 2010, Glasgow, UK, no. GT2010-22288.

[16] Ireland, P. T., and Jones, T. V., 2000. "Liquid Crystal Measurements of Heat Transfer and Surface Shear Stress". *Measurement Science & Technology*, ***11***(7), pp. 969–986.

[17] Schultz, D., and Jones, T., 1973. "Heat Transfer Measurements in Short Duration Hypersonic Facilities". *NATO Advisory Group Aeronautical RD AGARDograph*, ***165***.

[18] Ekkad, S. V., and Han, J. C., 2000. "A Transient Liquid Crystal Thermography Technique for Gas Turbine Heat Transfer Measurements". *Measurement Science & Technology*, ***11***(7), pp. 957–968.

[19] Poser, R., von Wolfersdorf, J., and Lutum, E., 2007. "Advanced Evaluation of Transient Heat Transfer Experiments Using Thermochromic Liquid Crystals". *Proceedings of the Institution of Mechanical Engineers Part A - Journal of Power and Energy*, ***221***(A6), pp. 793–801.

[20] Hoefler, F., Dietrich, N., and von Wolfersdorf, J., 2010. "Heat Transfer Experiments in a Confined Jet Impingement Configuration Using Transient Techniques". In Proceedings of the 14th International Heat Transfer Conference, August 8-13, 2010, Washington, DC, USA, no. IHTC14-22305.

[21] Moffat, R. J., 1988. "Describing the Uncertainties in Experimental Results". *Experimental Thermal and Fluid Science*, ***1***(1), pp. 3–17.

[22] Kingsley-Rowe, J. R., Lock, G. D., and Owen, J. M., 2005. "Transient Heat Transfer Measurements Using Thermochromic Liquid Crystal: Lateral-Conduction Error". *International Journal of Heat and Fluid Flow*, ***26***(2), pp. 256–263.

[23] Hofmann, H. M., Kaiser, R., Kind, M., and Martin, H., 2007. "Calculations of Steady and Pulsating Impinging Jets - an Assessment of 13 Widely Used Turbulence Models". *Numerical Heat Transfer Part B - Fundamentals*, ***51***(6), pp. 565–583.

[24] Rao, G., Kitron-Belinkov, M., and Levy, Y., 2009. "Numerical Analysis of a Multiple Jet Impingement System". In Proceedings of ASME Turbo Expo 2009, June 8-12, 2009, Orlando, Florida, USA, no. GT2009-59719.

[25] Zu, Y. Q., Yan, Y. Y., and Maltson, J., 2009. "Numerical Study on Stagnation Point Heat Transfer by Jet Impingement in a Confined Narrow Gap". *Journal of Heat Transfer*, ***131***(9), Sept., p. 094504.

[26] Roache, P. J., 1994. "Perspective - A Method for Uniform Reporting of Grid Refinement Studies". *Journal of Fluids Engineering*, ***116***(3), pp. 405–413.

